Article

High-Entropy Composite Coating Based on AlCrFeCoNi as an Anode Material for Li-Ion Batteries

Dávid Csík [1,2], Gabriela Baranová [1,*], Róbert Džunda [2], Dóra Zalka [2,3], Ben Breitung [4], Mária Hagarová [1] and Karel Saksl [1]

1   Institute of Materials and Quality Engineering, Faculty of Materials, Metallurgy and Recycling, Technical University of Košice, Letná 9, 042 00 Košice, Slovakia; dcsik@saske.sk (D.C.)
2   Institute of Materials Research, Slovak Academy of Sciences, Watsonova 47, 040 01 Košice, Slovakia
3   Department of Physics of Condensed Matters, Faculty of Sciences, Pavol Jozef Šafárik University in Košice, Park Angelinum 9, 041 54 Košice, Slovakia
4   Nanomaterials for Electronic and Energy Applications, Karlsruhe Institute of Technology (KIT), Institute of Nanotechnology, Hermann-von-Helmholtz-Platz 1, 76344 Eggenstein-Leopoldshafen, Germany
*   Correspondence: gabriela.baranova@tuke.sk

Abstract: In this study, a high entropy composite coating was synthesized by oxidizing a high entropy alloy, AlCrFeCoNi, at elevated temperatures in a pure oxygen atmosphere. X-Ray diffraction (XRD) analysis revealed that the prepared material was a dual-phase composite material consisting of a spinel-structured high entropy oxide and a metallic phase with a face-centered cubic structure. The metallic phase can improve the electrical conductivity of the oxide phase, resulting in improved electrochemical performance. Scanning electron microscopy with energy dispersive spectroscopy (SEM/EDS) analysis unveiled the compositional homogeneity of the composite material. The prepared material was utilized as an anode active material in lithium-ion batteries. Cyclic voltammetry (CV) revealed the oxidation and reduction regions, while the electrochemical impedance spectroscopy (EIS) measurements showed a decrease in the charge transfer resistance during the cycling process. A long-term rate capability test was conducted at various current densities: 100, 200, 500, 1000, and 2000 mA g^{-1}. During this test, a notable phenomenon was observed in the regeneration process, where the capacity approached the initial discharge capacity. Remarkably, a high regeneration efficiency of 98% was achieved compared with the initial discharge capacity. This phenomenon is typically observed in composite nanomaterials. At a medium current density of 500 mA g^{-1}, an incredible discharge capacity of 543 mAh g^{-1} was obtained after 1000 cycles. Based on the results, the prepared material shows great potential for use as an anode active material in lithium-ion batteries.

Keywords: lithium-ion battery; anode material; high entropy oxide; spinel oxide

1. Introduction

Lithium-ion batteries represent a method of energy storage due to high working potential differences at a high energy density. These characteristics determine their use in applications such as portable electronics, robotics, transport, etc. Due to their high energy efficiency, it is also possible to use them in various electric grid applications, including improving the quality and storage of energy obtained from various renewable energy sources such as wind, solar, and geothermal. This contributes to their better utilization and to building an energetically sustainable economy. To accelerate the utilization of renewable energy sources, research and innovation on lithium-ion batteries (LIBs) are encouraged to generate even higher energy density and higher power density while improving safety [1–4].

The main Li-ion battery components are the cathode, anode, separator, and electrolyte. Through research and development of these components, it is possible to achieve an improvement in the overall properties of the battery cell.

The requirement on the anode is to have a low working potential with high reducing power and low weight. The currently commercialized graphite anode is limited by its relatively low theoretical capacity (372 mAh g^{-1}) and the slow diffusion of lithium-ion. Therefore, some of the studies on the research and development of LIBs are focused on the development and optimization of the anode [4].

Silicon is a promising anode material as its theoretical capacity can reach 4200 mAh g^{-1}. However, the lithiation/de-lithiation process in silicon anode causes huge volume expansion and structural damage, which are accompanied by mechanical instability of the electroactive material and the SEI layer formed on the anode [5]. Other materials used as active anode materials are lithium-containing alloys such as Li-Sn, Li-Pb, Li-Al, Li-Zn, Li-Bi, Li-Ga, Li-In, and Li-Si; however, they also suffer from volume change during the charging/discharging process [6].

Transition metal oxides have also been intensively investigated as active anode materials as they have interesting electrochemical properties in LIBs and can have reversible capacities ranging from 500 to 1000 mAh g^{-1} [1,7]. Single-cation oxides based on transition metals were doped with foreign atoms with the aim of solving the volume change issue causing the disintegration of electrodes during cycling and achieving enhanced structure stability and increased cyclic stability [8].

To further improve the electrochemical performance of metal oxides, high entropy oxides (HEOs) were introduced as a novel promising active anode material for LIBs. The fast growth of the field of HEO is being facilitated by the availability of many synthesis and processing routes, which were shown to provide highly reproducible material systems [9].

HEOs can be synthesized by oxidizing high entropy alloys (HEAs). There are two essential definitions of a HEA [10]:

1. An alloy that consists of at least five major metallic elements, each having a concentration of 5%–35%.
2. An alloy whose configurational entropy is larger than 1.61*R, where R is the gas constant.

Each element system can have a different structure, such as body-centered cubic, face-centered cubic, or hexagonal. The more elements participate, the more functions can act simultaneously, assuming the formation of a multi-element compound with excellent overall properties [11,12].

HEOs usually crystallize into rocksalt, perovskite, or spinel structure. The stabilization effect of entropy has significant benefits on the storage capacity retention of HEOs and improves cycling stability [9]. HEOs show multiple quality characteristics such as super-high structural stability, high dielectric constant, and high ionic conductivity [8]. However, the electrochemical properties of high-entropy oxides have been observed to depend on each of the metal cations present, providing an opportunity to modify the electrochemical properties by simply changing the oxide composition [1,9,13,14].

A variety of binary and multi-element oxides have been studied as anodes for LIBs, which provide the exchange of lithium ions via a conversion reaction. Oxides with a spinel structure showed great potential for such use [15]. Cations in oxides with a spinel structure are in different oxidation states and ensure the three-dimensional transport of lithium ions. A higher number of oxidation states promotes the formation of oxygen vacancies, which provide favorable conditions for the transport of lithium ions and can ensure high charging and discharging rates. In HEOs consisting of at least five cations, this range is many times higher as a synergetic effect occurs between the different elements [4,15–17].

In general, the performance of HEO is controlled by the type and number of metal ions present in the structure. Therefore, the particular combination of metal ions used is essential [18].

To the best of our knowledge, the AlCrFeCoNi alloy and its spinel oxide have not been tested in lithium-ion batteries, making them an unexplored material system in this application. The inactivity of Al^{3+} within the voltage range of 0–3V vs. Li/Li^{+} [19–25] can potentially promote the spectator effect, similar to Mg^{2+} in rocksalt high entropy

oxides, contributing to enhanced cycling stability and inhibition of active nanograins agglomeration [9,26,27]. This study deals with the possible synthesis of AlCrFeCoNi alloy and its composite material consisting of a spinel oxide and metallic phase and their characterization, as well as testing the electrochemical properties of the prepared high entropy material (HEM) as a potential anode for a battery cell.

2. Materials and Methods

2.1. Material Synthesis

The choice of the elements used (Al, Cr, Fe, Co, Ni) was based on the theory of the formation of high entropy alloys discussed in [28–30]. According to these, the mixing enthalpy (ΔH_{mix}), entropy (ΔS_{mix}), and atomic size difference (δ) should be in the range $-22 \leq \Delta H_{mix} \leq 7$ kJ mol^{-1}, $11 \leq \Delta S_{mix} \leq 19.5$ J (K mol)$^{-1}$, $-0 \leq \delta \leq 8.5$. These values are met in the case of the AlCrFeCoNi alloy of equiatomic concentration: $\Delta H_{mix} = -12.32$ kJ mol^{-1}, $\Delta S_{mix} = 13.38$ J (K mol)$^{-1}$, $\delta = 5.77$.

The high entropy composite material based on AlCrFeCoNi was synthesized via a two-step process. First, a high entropy alloy, AlCrFeCoNi, was prepared by arc melting of pure elements in an argon atmosphere. Pure elements, Al (99.9%), Cr (99.9%), Fe (99.9%), Co (99.9%), and Ni (99.9%) were purchased from Alfa Aesar (ThermoFisher, Kandel, Germany). The elements were weighted in equiatomic concentration, except aluminum, which was overweighted because of its high evaporation during arc melting. The samples were re-melted five times to ensure as much chemical homogeneity as possible. After the melting process, the alloy pieces (3 g) were milled in a vibration mill at 30 Hz for 15 min using a steel jar and steel milling elements to minimize contamination. The obtained powder particles were sieved to get particles under 40 microns.

The AlCrFeCoNi powder particles were oxidized in a tube furnace at 1000 °C in a technically pure oxygen atmosphere for 5 h using Al_2O_3 ceramic boats. After the oxidation process, the sample was removed from the tube furnace and cooled on a steel plate. The sintered powder was milled in a vibration mill at 30 Hz for 30 s. The oxide powder particles were sieved to get particles under 40 microns.

2.2. Material Characterization

Phase analysis of the alloy and oxide was performed by X-Ray diffraction (XRD) using a laboratory X-Ray diffractometer Philips X'Pert Pro (Philips, Amsterdam, The Netherlands) in reflection mode operated at 40 kV and 50 mA using Cu Kα radiation with a scan step 0.03°, time per step 60 s, and 2 θ range of 15–140°. The morphology and size distribution of the powder particles and prepared electrodes were analyzed using a Tescan VEGA 3 LMU scanning electron microscope (Tescan, Brno, The Czech Republic) equipped with energy-dispersive X-Ray spectroscopy (Bruker, Billerica, MA, USA) to determine the chemical composition of the samples. The Rietveld refinement of the XRD data was performed using GSAS II software (Argonne National Laboratory, Lemont, IL, USA) (version GSAS V5556) [31,32].

2.3. Coin Cell Preparation

The prepared AlCrFeCoNi high entropy composite material was used as an anode active material in different electrochemical cells (CR2032, El-Cell, and 2-electrode Swagelok cell). The electrode preparation process consisted of several steps. The prepared high entropy material (70 wt. %) together with carbon black Super P (20 wt. %) and polyvinylidene fluoride PVDF (10 wt. %) dissolved in N-methyl pyrrolidone (NMP) were mixed using a Thinky ARE-250 mixer. The slurry was cast onto a Cu foil and dried at 120 °C in a vacuum for 18 h. After the drying process, the electrodes were cut into disc electrodes with 13 mm diameters. Active material loading was about 1.13 mg cm^{-2}. After the electrode-cutting process, the electrodes were further dried at 120 °C. The half cells were assembled in an argon-filled glovebox with a controlled atmosphere ($O_2 < 1$ ppm, $H_2O < 1$ ppm). Metallic lithium, Whatman GF/A, and HEM electrode were used as a counter electrode, separator,

and working electrode, respectively. 1 M LiPF$_6$ dissolved in a mixture of ethylene carbonate and diethyl carbonate (EC/DEC) in a 1:1 volume ratio was used as an electrolyte.

2.4. Electrochemical Characterisation

Cyclic voltammetry (CV) test at a sweep rate of 0.1 mV s^{-1} in a potential range of 0.01–3 V vs. Li/Li$^+$ and electrochemical impedance spectroscopy (EIS) measurements in a frequency range of 100 kHz and 1 MHz were conducted on a BioLogic SP-150 potentiostat/galvanostat (BioLogic, Seyssinet-Pariset, France). The galvanostatic charge/discharge measurements were performed using a Landt Battery Cycler CT3002AU (Landt Instruments, New York, NY, USA) in a potential range of 0.01–3 V vs. Li/Li$^+$.

3. Results and Discussion

3.1. Material Characterization

Phase analysis revealed that the high-entropy alloy crystallized into a body-centered cubic structure with a space group of Im-3m and a lattice parameter of 2.870 Å, which is comparable to the findings in [33]. No additional phases were present. The Rietveld refinement of the alloy's structure is shown in Figure 1a. The weighted profile R-factor (Rwp) of 1.32% indicates a highly reliable refinement.
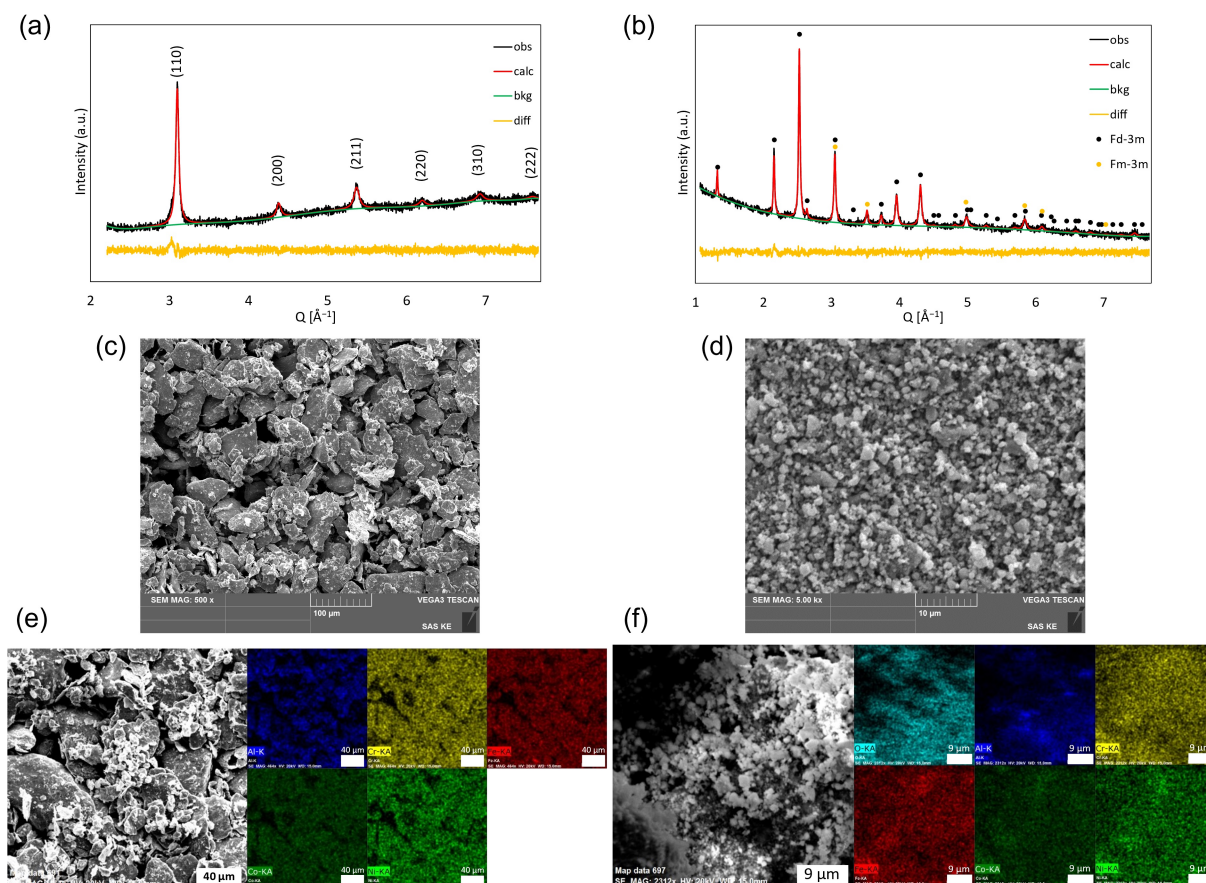

Figure 1. (**a**) Rietveld refined XRD pattern of HEA, Rwp = 1.32%, (**b**) Rietveld refined XRD pattern of HEM, Rwp = 1.28%, (**c**) SEM image of HEA powder, (**d**) SEM image of HEM powder, (**e**) EDS mapping of HEA powder, (**f**) EDS mapping of HEM powder.

The alloy powder particles had a rough, irregular morphology ranging from oval to rod-shaped structures, as shown in Figure 1c. The size distribution of the particles was non-uniform. The particle sizes of the rod-shaped structures ranged from approximately 1 μm to more than 100 μm. EDS analysis revealed that the elemental concentration was quasi-equiatomic (Table 1). The biggest deviation from the equiatomic concentration was

in the case of aluminum due to its high vapor pressure during arc melting [34]. Based on the elemental concentration, the configurational entropy is 1.604 R, indicating that the prepared alloy belongs to the high entropy alloy group [10]. According to the EDS mapping in Figure 1e, the various elements were found to be homogeneously distributed throughout the entire analyzed area of the prepared alloy, indicating a uniform elemental distribution.

Table 1. EDS analysis of HEA and HEM powder.

Element	HEA				HEM			
	wt.%	σ wt.%	at.%	σ at.%	wt.%	σ wt.%	at.%	σ at.%
Oxygen	-	-	-	-	27.28	0.51	54.12	0.64
Aluminum	7.15	2.95	13.69	5.51	7.93	0.08	9.33	0.15
Chromium	21.38	1.34	21.55	1.87	15.55	0.22	9.49	0.20
Iron	24.10	1.94	22.64	2.54	16.84	0.19	9.57	0.10
Cobalt	25.26	0.61	22.44	1.20	17.10	0.31	9.21	0.22
Nickel	22.11	0.99	19.69	0.77	15.31	0.06	8.28	0.09

During the oxidation process, the HEA powder particles transformed into a composite high entropy material and were free-sintered. Because of that, a milling process was applied to obtain powder particles of micrometer sizes. The powder particles exhibited a bimodal size distribution, with small particles ranging from 300 nm to 6 μm and larger particles ranging from 10 to 85 μm, as shown in Figure 1d. The particles had rough or irregular morphologies, but the elements were homogenously distributed throughout the analyzed area without any segregation (Figure 1f and Table 1).

Phase analysis of the HEM revealed that the material consisted of two phases, as shown in Figure 1b. The major phase had a cubic structure with a space group of Fd-3m and a lattice parameter of 8.267 Å belonging to the inverse spinel oxide group Me_3O_4 (space group 227:2) [35]. The minor phase had a cubic structure with a space group of Fm-3m and a lattice parameter of 3.575 Å, corresponding to a metallic group. The metallic content, determined by Rietveld refinement with Rwp = 1.28%, was approximately 9.8 wt.%. This can be attributed to the oxidation resistance of specific elements such as Cr and Al, which can form a passive oxide layer on the surface of the particles, hindering further oxidation [36–40]. In this case, it is likely that the larger particles were covered with this passive oxide layer, while the core of the particles remained metallic. However, a phase transformation of the metallic phase occurred from Im-3m to Fm-3m, similar to the transformation observed in [36–40]. According to [41], Fe, Co, and Ni possess high electronic conductivity in lithium-ion batteries, which makes them valuable for enhancing the electrical conductivity of materials with poor conductivity. Consequently, they are commonly utilized in the production of composite materials.

The most common and general formula used to calculate the configuration entropy of an $A_xB_yO_z$ oxide is [42]:

$$S_{conf} = -R\left[x\left(\sum_{a=1}^{M} x_a \ln x_a\right)_A + y\left(\sum_{b=1}^{N} y_b \ln y_b\right)_B + z\left(\sum_{o=1}^{P} z_o \ln z_o\right)_O\right] \tag{1}$$

In this equation, x_a, y_b, and z_o represent the mole fractions of elements in the A-site, B-site, and O-site, respectively. However, this formula cannot be applied to spinel-structured oxides because of the presence of two different Wyckoff sites for the cations (8a, 16d) that increases the entropy of the system. Therefore, a universal configurational entropy metric was formulated and described in [43,44]:

$$EM = S^{conf} \times L = -R\left[\frac{\sum ax \sum f_i^x \cdot \ln f_i^x}{\sum a^x}\right] \times L \tag{2}$$

In Equation (2), a^x represents the number of sites on the x sublattice, f_i^x is the fraction of element species i randomly distributed on the x sublattice (site fraction), L is the total number of sublattices, and R is the ideal gas constant. Materials can be classified into specific groups based on the configurational entropy, with high entropy materials denoted by EM > 1.5 R. For the $(Cr_{0.25}Fe_{0.25}Co_{0.25}Ni_{0.25})(Al_{0.6}Cr_{0.35}Fe_{0.35}Co_{0.35}Ni_{0.35})_2O_4$ spinel oxide (assuming Al is only present in +III oxidation state and all elements are in equimolar concentration), the EM value is 2.045 R, placing this spinel oxide in the high entropy group. Furthermore, the configurational entropy is significantly higher than that of an oxide with a rocksalt structure (1.61 R) [9,26,45], indicating increased structural stability and cyclability. However, it should be noted that this calculation is an approximation due to unknown distribution of different cation types in the two sublattices, and the EM represents the highest value for this system.

3.2. Electrochemical Characterization

To investigate the electrochemical properties of the composite HEM, cyclic voltammetry was performed in a potential range of 0.01–3 V vs. Li/Li$^+$ with a sweep rate of 0.1 mV s^{-1} for five cycles (Figure 2a). The first cycle exhibited several distinct reduction peaks, from 1.23 to 0.42 V, which can be attributed to a stepwise reduction of transition metal oxides from high valence state (M^{3+}) to low valence state (M^{2+}) and eventually to the metallic form (M^0) [4,8,46]. Considering that Al^{3+} is inactive within this potential range [19–25], it is presumed that it plays a stabilizing role similar to Mg^{2+} in rocksalt-structured high entropy oxides [9,26,27,47–49]. The most prominent reduction peak observed at 0 V is associated with the formation of solid electrolyte interphase (SEI) layer on the electrode surface due to electrolyte decomposition. During the first positive scan, a broad anodic peak ranging from 1.0 to 1.6 V vs. Li/Li$^+$ indicates the reoxidation of metallic phases to high-valence oxides [4,8,46]. In the subsequent cycles, the intensity of the major reduction peaks decreases, indicating the formation and slower growth of the SEI layer [4,8]. The CV curves from the 2nd cycle onwards exhibit similar shapes, suggesting good reversibility and cycling stability. The CV curve of this composite HEO is comparable to other high entropy oxides with a spinel structure [4,8,15,46,50]. Further investigation, such as in operando synchrotron XRD or X-Ray absorption spectroscopy (XAS) is required to fully understand the lithiation/delithiation mechanism in this composite system.

Figure 2b,c shows the complex-plane impedance plots of the coin cell with HEM electrode, Li metal anode, and 1 M LiPF$_6$ in a mixture of EC/DEC 50/50 electrolytes before and after five cycles. The electrochemical impedance measurements were carried out in the frequency range 100 kHz–100 MHz, with 10 mV sinusoid voltage perturbation at open circuit potential. To determine the initial parameters of the complex nonlinear least-squares (CNLS) fitting, distribution of relaxation times (DRT) analysis was performed as described in [51–53].

The first spectrum belongs to the as-prepared cell, where R$_s$ describes the solution resistance, Z$_{RQ1}$ is the contact resistance between the HEM electrode and the current collector, Z$_{RQ2}$ is the charge transfer resistance between the HEM and the electrolyte, and Z$_{RQ3}$ describes the resistance between the Li/electrolyte interface. The de Levie element was introduced due to the not completely flat surface of the HEM electrode [54].

The CNLS fitting was performed using a code written in Python 3 (Python Software Foundation, Wilmington, DE, USA) with standard scientific packages (NumPy, SciPy, Pandas, Lmfit, and Matplotlib). The results are shown in Figure 2b,c with the schematic drawing of the fitted model. The decreased resistances observed in this study after cycling can be attributed to the successful incorporation of the lithium ions into the HEO layer, leading to improved electrical connection and ionic percolation, resulting in reduced polarization (Table 2). The formation of the SEI layer led to a slight increase in resistance on the Li-electrolyte interface. The changes in the resistances observed here are in good agreement with the trends on HEO presented in the literature [47].
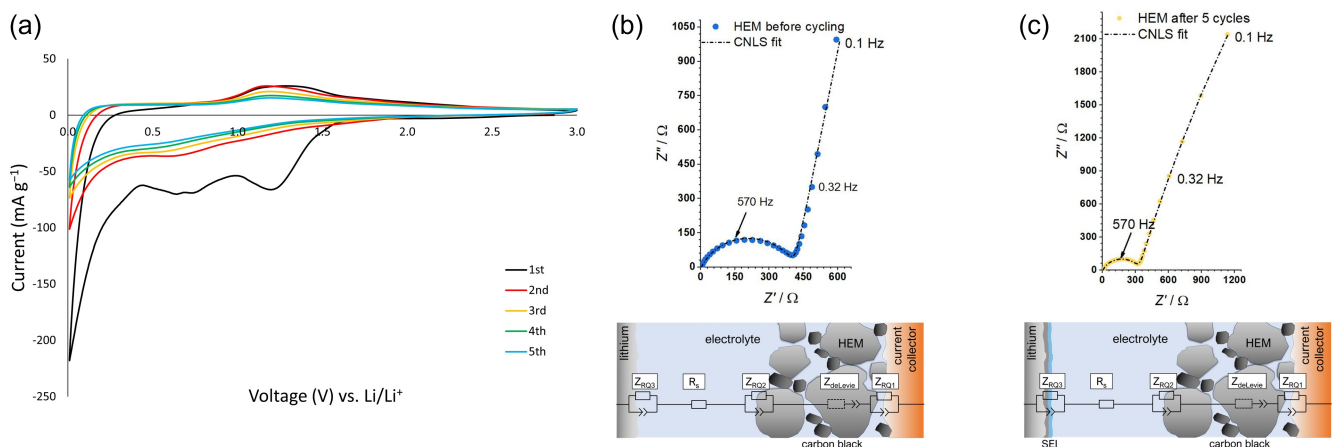
Figure 2. (**a**) CV curves at 0.1 mV s^{-1} from 0.1 to 3 V vs. Li/Li$^+$, Complex plane impedance plots (**b**) before and (**c**) after 5 cycles and the equivalent circuit representations of the corresponding models used to the CNLS fitting.

Table 2. Estimated values of the parameters and their standard error of CNLS fitting.

	HEM before Cycling		HEM after Cycling	
	$X^2/|Z| = 2.0341 \cdot 10^{-3}$		$X^2/|Z| = 6.2658 \cdot 10^{-4}$	
	Estimated Value	**Standard Error**	**Estimated Value**	**Standard Error**
R_s (Ohm)	3.60	$\pm 6.6613 \cdot 10^{-2}$	4.8253	± 0.2703
R_1 (Ohm)	147.179	± 3.0541	121.1729	± 2.9620
Q_1 (F)	$1.1875 \cdot 10^{-5}$	$\pm 3.6114 \cdot 10^{-7}$	$1.1387 \cdot 10^{-5}$	$\pm 3.1665 \cdot 10^{-7}$
n_1	0.710644	$\pm 3.3045 \cdot 10^{-2}$	0.90256	$\pm 1.1401 \cdot 10^{-3}$
R_2 (Ohm)	201.06802	$\pm 2.0223 \cdot 10^{-1}$	186.4122	$\pm 3.6832 \cdot 10^{-2}$
Q_2 (F)	$1.95700 \cdot 10^{-3}$	$\pm 2.2669 \cdot 10^{-5}$	$6.0293 \cdot 10^{-5}$	$\pm 7.6112 \cdot 10^{-1}$
n_2	0.731745	$\pm 7.8472 \cdot 10^{-3}$	0.7651	$\pm 9.5216 \cdot 10^{-3}$
R_3 (Ohm)	27.26705	$\pm 1.8926 \cdot 10^{-1}$	44.0167	$\pm 1.7065 \cdot 10^{-2}$
Q_3 (F)	$3.02459 \cdot 10^{-2}$	$\pm 3.4817 \cdot 10^{-3}$	$9.9871 \cdot 10^{-2}$	$\pm 1.8089 \cdot 10^{-3}$
n_3	0.613330	$\pm 2.0345 \cdot 10^{-2}$	0.6981	$\pm 3.5001 \cdot 10^{-3}$
R_{ion} (Ohm)	172.1767	$\pm 3.6627 \cdot 10^{-1}$	55.6004	$\pm 1.9780 \cdot 10^{-1}$
Q_s (F)	$1.67485 \cdot 10^{-4}$	$\pm 4.0219 \cdot 10^{-5}$	$6.3282 \cdot 10^{-4}$	$\pm 1.6962 \cdot 10^{-5}$
γ	0.91243	$\pm 5.0066 \cdot 10^{-4}$	0.8006	$\pm 4.4166 \cdot 10^{-3}$

Figure 3a illustrates the long-term cyclic performance at a current density of 100 mA g^{-1}. The initial discharge and charge capacities were 757 and 475 mAh g^{-1}, respectively, resulting in a low Coulombic efficiency of 63.3%. This is attributed to the formation of the solid electrolyte interphase layer, which consumes active lithium ions and electrolyte materials, leading to capacity fading [55]. The initial discharge voltage profile in the first cycle, as shown in Figure 3b, exhibits a rapid potential decrease from 3 down to 1 V, followed by a moderate decrease, consistent with the CV curve and corresponding to the reduction of metallic cations to metal phases [4,16,17]. From the second cycle onwards, the voltage profile shows similar shapes, indicating that the SEI formation is completed or not as significant as in the first cycle [17,45,56]. However, the capacity slightly decreases in each cycle until the 55th cycle, reaching a minimum capacity of 383 mAh g^{-1}. This capacity fading can be attributed to the growth of the SEI layer, transition metal dissolution, mechanical cracking, volume changes, electrolyte depletion, and Li plating [57,58]. Subsequently, the capacity starts to rise, reaching a maximum value of 695 mAh g^{-1} at the 200th cycle. This phenomenon can be attributed to changes in the morphology of the powder particles. The application of mechanical stress caused by rapid volume expansion during lithiation can lead to fractures that increase the active surface area. These morphological

changes enhance reaction kinetics by improving transport, ultimately resulting in an increase in specific capacity. This phenomenon, known as the reactivation of electrochemical reactions, induced by high-rate lithiation, leads to an increase in capacity during high-rate cycling [57].
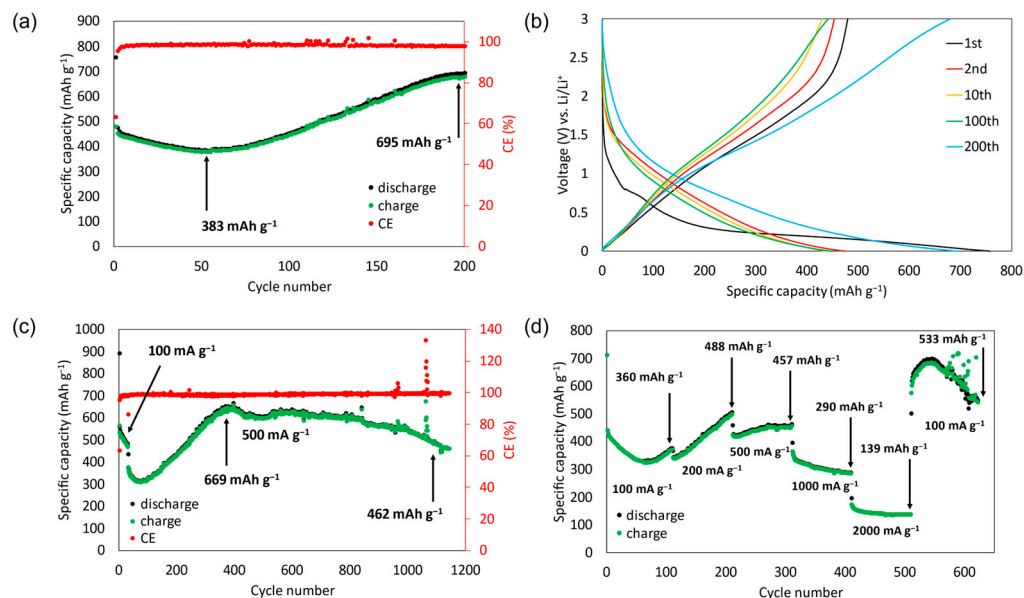

Figure 3. Half-cell performance of HEM: (**a**) long-term cycling at a current density of 100 mA g^{-1}, (**b**) charge/discharge voltage profiles of HEM for the 1st, 2nd, 10th, 100th, and 200th cycles in the voltage range 0.01–3 V vs. Li/Li$^+$ at a current density of 100 mA g^{-1}, (**c**) long-term cycling of HEM at a current density of 500 mA g^{-1} with 30 formation cycles at a current density of 100 mA g^{-1}, (**d**) long-term rate capability test of HEM at various current densities (100, 200, 500, 1000, and 2000 mA g^{-1}) with 100 cycles each. Regeneration was performed at a current density of 100 mA g^{-1} for 100 cycles.

For long-term cycling at a medium current density of 500 mA g^{-1}, a formation process was applied to the cell at 100 mA g^{-1} for 30 cycles to stabilize the SEI layer [9], as shown in Figure 3c. During the formation cycles, the same capacity decrease as in the previous case was observed. At 500 mA g^{-1}, the capacity fading continued until the 70th cycle, reaching a minimum capacity of 315 mAh g^{-1}. After that, the capacity started to increase, reaching an outstanding value of 669 mAh g^{-1}. Higher capacities in similar slurry ratios were observed only in a few high entropy oxides of nanometer sizes [11,16,17,26]. For the following 400 cycles, the capacity remained relatively stable at 600 mAh g^{-1}. After the 800th cycle, the capacity started to fade but remained at 462 mAh g^{-1} after 1100 cycles, which is 70% of the maximum value. A capacity fluctuation can be observed for five cycles around the 1060 s cycles, after which the capacity fading stabilized. This behavior can be attributed to structural changes associated with the active material [9]. These results indicate excellent cyclic stability even at medium current densities.

The rate capability test was performed in a specific manner to account for the observed changes in the capacity during cycling, as described earlier. As a result, the test was conducted at different current densities, with each density tested for 100 cycles, as shown in Figure 3d. At 100 mA g^{-1}, the same capacity fading and the subsequent increase described earlier was observed. At 200 mA g^{-1}, the capacity increase was monotonous due to the morphological changes [57]. At 500 mA g^{-1}, the capacity increase was also monotonous but the slope was more moderate, indicating that at higher current densities, the achievable capacity could be reduced due to polarization and diffusion limitations [59]. At 1000 mA g^{-1}, a monotonous decrease in capacity was observed, while the capacity remained stable for 100 cycles at 2000 mA g^{-1}. These specific capacities at different current

densities are comparable to the capacities of single-phase high entropy oxides of nanometer sizes [4,15]. The capacities were: 360, 488, 457, 290, and 139 mAh g^{-1} at current densities of 100, 200, 500, 1000, and 2000 mA g^{-1}, respectively. An interesting phenomenon occurred during the regeneration process at an initial current density of 100 mA g^{-1}. The capacity in the first cycle of the regeneration process reached the same level as the maximum capacity at 200 mA g^{-1}. Subsequently, the capacity increased to a maximum value of 698 mA h^{-1}, which is very close to the initial discharge capacity of 712 mAh g^{-1}, resulting in a regeneration efficiency of 98%. After reaching the maximum capacity, it started to fade, but even after 100 cycles in the regeneration process (a total of 600 cycles), the capacity was 533 mAh g^{-1}, which is 75% of the initial discharge capacity, indicating the excellent self-healing properties of this material. This kind of capacity regeneration compared with the initial discharge capacity has not been observed in high entropy oxides with a spinel structure. The average regeneration efficiency is approximately 45%–50% in the case of spinel-structured HEOs [4,15]. To the best of our knowledge, a higher efficiency of the regeneration process (79%) has only been achieved in a high entropy oxide with a rocksalt structure [9]. Further research is needed to fully understand the reasons behind this phenomenon.

In comparison to previous studies, HEM based on AlCrFeCoNi demonstrates enhanced electrochemical properties, despite having particle sizes in the micrometer range, as shown in Table 3. In rate capability tests conducted at both low and high current densities, HEM based on AlCrFeCoNi exhibits the lowest specific capacity. However, at a medium current density of 500 mA g^{-1}, the capacity is comparable to that of materials containing five active elements and having particle sizes in the nanometer range.

Table 3. Comparisons of electrochemical properties of high entropy oxides.

Material	Particle Size	Long-Term Cycling	Rate Capability Test-Specific Capacities (mAh g^{-1}) at Current Densities						Reference
			100 mA g^{-1}	200 mA g^{-1}	500 mA g^{-1}	1000 mA g^{-1}	2000 mA g^{-1}	100 mA g^{-1}	
(CrMnFeCoNi)$_3$O$_4$	200–900 nm	402 mAh g^{-1} at 500 mA g^{-1} (300 cycles)	586	478	361	269	180	483	[4]
(CrMnFeCoNi)$_3$O$_4$	200–500 nm	693 mAh g^{-1} at 500 mA g^{-1} (260 cycles)	967	828	740	625	532	837 at 200 mA g^{-1}	[11]
(CrMnFeCoNi)$_3$O$_4$	100–200 nm	750 mAh g^{-1} at 500 mA g^{-1} (200 cycles)	1072	979	824	649	500	-	[16]
(MgTiZnCuFe)$_3$O$_4$	51–345 nm	504 mAh g^{-1} at 100 mA g^{-1} (300 cycles)	571	460	405	342	268	552	[15]
(CrMnFeNiCu)$_3$O$_4$	500–800 nm	512 mAh g^{-1} at 500 mA g^{-1} (250 cycles)	567	482	400	297	226	-	[50]
(TiMnFeCoNi)$_3$O$_4$	micrometer sizes	536 mAh g^{-1} at 100 mA g^{-1} (100 cycles)	496	455 at 250 mA g^{-1}	435	401	343 at 2500 mA g^{-1}	590 at 50 mA g^{-1}	[56]
(MgCrMnFeCo)$_3$O$_4$	50 nm	673 mAh g^{-1} at 1000 mA g^{-1} (1000 cycles)	964	892	787	658	541	594	[60]
(AlCrFeCoNi)$_3$O$_4$	micrometer sizes	543 mAh g^{-1} at 500 mA g^{-1} (1000 cycles)	360	488	457	290	139	533	This study

One of the most notable properties of HEM based on AlCrFeCoNi is its regeneration efficiency, where it can deliver 1.5 times higher capacity compared to the initial cycling capacity. Furthermore, even after 1000 cycles at a current density of 500 mA g^{-1}, the capacity of HEM based on AlCrFeCoNi remains higher compared to several high entropy oxides with nanometer-sized particles.

It is important to consider that direct comparisons between studies may be influenced by variations in experimental conditions, synthesis methods, and characterization techniques employed. Nevertheless, these findings highlight the significant electrochemical advancements achieved by our material, indicating its potential for various applications in the field.

3.3. Electrode Surface Characterization

The structural changes in the electrodes before and after cycling can be seen in Figure 4a–f. The electrodes underwent 20 cycles at a current density of 100 mA g^{-1} and their macro and microstructures were observed before and after cycling. Before cycling, the electrode surface appeared relatively homogeneous and compact. Larger particles (above 10 μm) of high entropy material were evenly distributed across the electrode surface, indicating that the slurry-making process and casting were not affected by these particles. However, smaller cracks surrounding these larger oxide particles were observed, suggesting some structural weaknesses due to the rigidity of the PVDF [61]. These cracks formed during drying at an elevated temperature of 120 °C as a result of internal stresses in the composite coating [62]. EDS analysis revealed the presence of various elements in the electrode composition. The high entropy material elements (Co, Fe, Cr, Ni, Al, O) were uniformly distributed across the entire electrode surface. Additionally, carbon and fluorine from polyvinylidene fluoride were also found to be uniformly distributed. After cycling, a notable change was observed on the electrode surface. It was covered by glass fibers originating from the separator material. However, no film breakage or peeling-off was observed. Larger oxide particles remained uniformly distributed across the electrode surface after cycling, but their abundance and size were smaller compared to the pristine electrode surface. This reduction in particle size and abundance indicates the breaking of agglomerates, which can be attributed to the repeated processes of reduction and oxidation during charging and discharging [57]. During cycling, pre-existing cracks in the electrode structure expanded and grew throughout the electrode surface. This increase in cracks was caused primarily by differences in the contraction and expansion coefficients between the metallic and oxide phases present in the electrode [11,45,63]. Consequently, the overall capacity of the electrode decreased due to the presence of these cracks. Examining the distribution of the elements after cycling showed that all the present elements were uniformly distributed across the electrode surface, indicating that no segregation occurred during the cycling process [50].
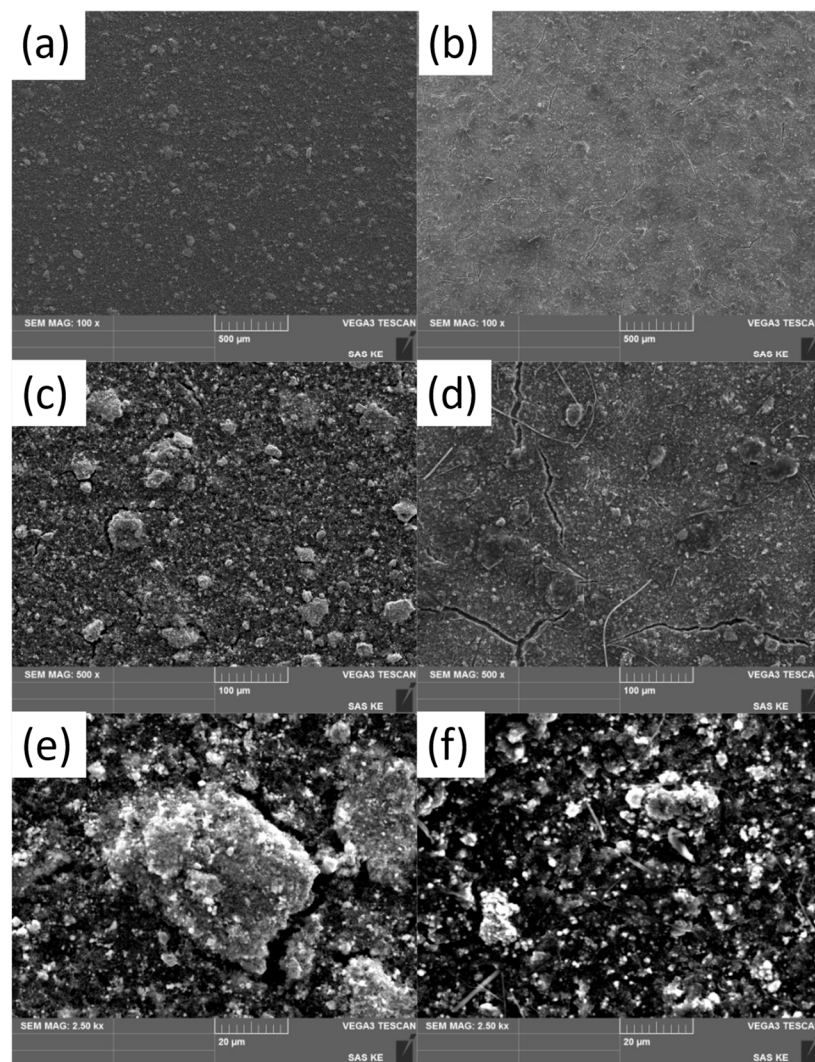
Figure 4. SEM images of the prepared electrode surfaces before (**a**,**c**,**e**) and after (**b**,**d**,**f**) 20 cycles at a current density of 100 mA g^{-1}.

4. Conclusions

In this study, a simple and rare method was employed to synthesize a high entropy material through oxidation of a high entropy alloy at elevated temperatures in a pure oxygen atmosphere.

The prepared single-phase high entropy alloy AlCrFeCoNi possesses a cubic structure and belongs to the high entropy alloy group based on its configurational entropy. During the oxidation process, the high entropy alloy transformed into a dual-phase composite material consisting of a spinel oxide and residual metallic phase with a face-centered cubic structure.

Despite its dual-phase character, the high entropy composite material based on AlCrFeCoNi was successfully utilized in lithium-ion batteries as an anode active material. The electrode surface exhibited a homogeneous and compact structure with larger particles of high entropy material uniformly distributed across the electrode surface. A decrease in charge transfer resistance was observed after five cycles, indicating the successful incorporation of the lithium ions into the high entropy material layer. Excellent cyclic stability was successfully achieved during long-term cycling at a medium current density. Long-term cyclic measurements revealed a phenomenon, where a moderate increase in capacity occurred during cycling. At a medium current density of 500 mA g^{-1}, a discharge capacity of 543 mAh g^{-1} was obtained after 1000 cycles. In the rate capability test, a regeneration

efficiency of 98% was achieved in the regeneration process relative to the initial discharge capacity.

No breaking or peeling of the coating was observed after cycling.

This study has shed light on the utilization of a high entropy composite material as an anode material for lithium-ion batteries, obtaining initial discharge capacities and preserving high capacities during long-term cycling.

Author Contributions: Conceptualization, D.C. and G.B.; methodology, D.C.; software, D.Z.; validation, D.C., D.Z. and R.D.; formal analysis, D.C., G.B., R.D. and D.Z.; investigation, D.C., G.B., R.D., D.Z. and M.H.; resources, B.B., M.H. and K.S.; data curation, D.C. and D.Z.; writing—original draft preparation, D.C. and G.B.; writing—review and editing, D.C., G.B., R.D., D.Z., B.B., M.H. and K.S.; visualization, D.C. and G.B.; supervision, B.B. and K.S.; project administration, D.C. and G.B.; funding acquisition, D.C. and K.S. All authors have read and agreed to the published version of the manuscript.

Institutional Review Board Statement: Not applicable.

Informed Consent Statement: Not applicable.

Data Availability Statement: Data is contained within the article.

Conflicts of Interest: The authors declare no conflict of interest.

References

1. Nitta, N.; Wu, F.; Lee, J.T.; Yushin, G. Li-ion battery materials: Present and future. *Mater. Today* **2015**, *18*, 252–264. [CrossRef]
2. Ma, S.; Jiang, M.; Tao, P.; Song, C.; Wu, J.; Wang, J.; Deng, T.; Shang, W. Temperature effect and thermal impact in lithium-ion batteries: A review. *Prog. Nat. Sci. Mater. Int.* **2018**, *28*, 653–666. [CrossRef]
3. Zhang, W.J. A review of the electrochemical performance of alloy anodes for lithium-ion batteries. *J. Power Sources* **2011**, *1*, 13–24. [CrossRef]
4. Wang, D.; Jiang, S.; Duan, C.; Mao, J.; Dong, Y.; Dong, K.; Wang, Z.; Luo, S.; Liu, Y.; Qi, X. Spinel-structured high entropy oxide (FeCoNiCrMn)$_3$O$_4$ as anode towards superior lithium storage performance. *J. Alloys Compd.* **2020**, *844*, 156158. [CrossRef]
5. Wu, F.; Chu, F.; Xue, Z. Lithium-Ion Batteries. In *Encyclopedia of Energy Storage*; Elsevier: Oxford, UK, 2022; Volume 4, pp. 5–13. [CrossRef]
6. Gu, X.; Dong, J.; Lai, C. Li-containing alloys beneficial for stabilizing lithium anode: A review. *Eng. Rep.* **2020**, *3*, e12339. [CrossRef]
7. Fang, S.; Bresser, D.; Passerini, S. Transition Metal Oxide Anodes for Electrochemical Energy Storage in Lithium- and Sodium-Ion Batteries. *Adv. Energy Mater.* **2019**, *10*, 1902485. [CrossRef]
8. Duan, C.; Tian, K.; Li, X.; Wang, D.; Sun, H.; Zheng, R.; Wang, Z.; Liu, Y. New spinel high-entropy oxides (FeCoNiCrMnXLi)$_3$O$_4$ (X = Cu, Mg, Zn) as the anode material for lithium-ion batteries. *Ceram. Int.* **2021**, *47*, 32025–32032. [CrossRef]
9. Sarkar, A.; Velasco, L.; Wang, D.; Wang, Q.; Talasila, G.; de Biasi, L.; Kübel, C.; Brezesinski, T.; Bhattacharya, S.S.; Hahn, H.; et al. High entropy oxides for reversible energy storage. *Nat. Commun.* **2018**, *9*, 3400. [CrossRef]
10. Zhang, Y. *High-Entropy Materials*, 1st ed.; Springer Nature Singapore Pte Ltd.: Singapore, 2019; pp. 12–25. [CrossRef]
11. Xiao, B.; Wu, G.; Wang, T.; Wei, Z.; Sui, Y.; Shen, B.; Qi, J.; Wei, F.; Zheng, J. High-entropy oxides as advanced anode materials for long-life lithium-ion Batteries. *Nano Energy* **2022**, *95*, 106962. [CrossRef]
12. Wang, Q.; Sarkar, A.; Wang, D.; Velasco, L.; Azmi, R.; Bhattacharya, S.S.; Bergfeldt, T.; Düvel, A.; Heitjans, P.; Brezesinski, T.; et al. Multi-anionic and -cationic compounds: New high entropy materials for advanced Li-ion batteries. *Energy Environ. Sci.* **2019**, *12*, 2433–2442. [CrossRef]
13. Ji, L.; Lin, Z.; Alcoutlabi, M.; Zhang, X. Recent developments in nanostructured anode materials for rechargeable lithium-ion batteries. *Energy Environ. Sci.* **2011**, *4*, 2682–2699. [CrossRef]
14. Musicó, B.L.; Gilbert, D.; Ward, T.Z.; Page, K.; George, E.; Yan, J.; Mandrus, D.; Keppens, V. The emergent field of high entropy oxides: Design, prospects, challenges, and opportunities for tailoring material properties. *APL Mater.* **2020**, *8*, 040912. [CrossRef]
15. Chen, H.; Qiu, N.; Wu, B.; Yang, Z.; Sun, S.; Wang, Y. A new spinel high-entropy oxide (Mg$_{0.2}$Ti$_{0.2}$Zn$_{0.2}$Cu$_{0.2}$Fe$_{0.2}$)$_3$O$_4$ with fast reaction kinetics and excellent stability as an anode material for lithium-ion batteries. *RSC Adv.* **2020**, *10*, 9736–9744. [CrossRef]

16. Nguyen, T.X.; Patra, J.; Chang, J.K.; Ting, J.M. High entropy spinel oxide nanoparticles for superior lithiation-delithiation performance. *J. Mater. Chem. A* **2020**, *8*, 18963–18973. [CrossRef]
17. Huang, C.-Y.; Huang, C.-W.; Wu, M.-C.; Patra, J.; Nguyen, T.X.; Chang, M.-T.; Clemens, O.; Ting, J.-M.; Li, J.; Chang, J.-K.; et al. Atomic-scale investigation of Lithiation/Delithiation mechanism in High-entropy spinel oxide with superior electrochemical performance. *Chem. Eng.* **2021**, *420*, 129838. [CrossRef]
18. Wang, X.L.; Jin, E.M.; Sahoo, G.; Jeong, S.M. High-Entropy Metal Oxide ($NiMnCrCoFe)_3O_4$ Anode Materials with Controlled Morphology for High-Performance Lithium-Ion Batteries. *Batteries* **2023**, *9*, 147. [CrossRef]
19. Han, B.; Paulauskas, T.; Key, B.; Peebles, C.; Park, J.S.; Klie, R.F.; Vaughey, J.T.; Dogan, F. *CS* Understanding the Role of Temperature and Cathode Composition on Interface and Bulk: Optimizing Aluminum Oxide Coatings for Li-Ion Cathodes. *Appl. Mater. Interfaces* **2017**, *9*, 14769–14778. [CrossRef]
20. Casino, S.; Heidrich, B.; Makvandi, A.; Beuse, T.; Gallasch, T.; Peterlechner, M.; Wilde, G.; Winter, M.; Niehoff, P. Al_2O_3 protective coating on silicon thin film electrodes and its effect on the aging mechanism of lithium metal and lithium ion cells. *J. Energy Storage* **2021**, *44*, 103479. [CrossRef]
21. Friesen, A.; Hildebrand, S.; Horsthemke, F.; Börner, M.; Klöpsch, R.; Niehoff, P.; Schappacher, F.M.; Winter, M. Al_2O_3 coating on anode surface in lithium ion batteries: Impact on low temperature cycling and safety behavior. *J. Power Sources* **2017**, *363*, 70–77. [CrossRef]
22. Lee, J.; Amari, H.; Bahri, M.; Shen, Y.; Xu, C.; Ruff, Z.; Grey, C.P.; Ersen, O.; Aguadero, A.; Browning, N.D.; et al. The Complex Role of Aluminium Contamination in Nickel-Rich Layered Oxide Cathodes for Lithium-Ion Batteries. *Batt. Supercaps* **2021**, *4*, 1813–1820. [CrossRef]
23. Jung, S.; Han, Y.-K. How Do Li Atoms Pass through the Al_2O_3 Coating Layer during Lithiation in Li-ion Batteries? *J. Phys. Chem. Lett.* **2013**, *4*, 2681–2685. [CrossRef]
24. Zheng, Y.; Wu, X.; Lan, X.; Hu, R. A Spinel $(FeNiCrMnMgAl)_3O_4$ High Entropy Oxide as a Cycling Stable Anode Material for Li-Ion Batteries. *Processes* **2022**, *10*, 49. [CrossRef]
25. Guo, M.; Liu, Y.; Zhang, F.; Cheng, F.; Cheng, C.; Miao, Y.; Gao, F.; Yu, J. Inactive Al^{3+}-doped $La(CoCrFeMnNiAlx)_{1/(5+x)}O_3$ high-entropy perovskite oxides as high performance supercapacitor electrodes. *J. Adv. Ceram.* **2022**, *11*, 742–753. [CrossRef]
26. Qiu, N.; Chen, H.; Yang, Z.; Sun, S.; Wang, Y.; Cui, Y. A high entropy oxide ($Mg_{0.2}Co_{0.2}Ni_{0.2}Cu_{0.2}Zn_{0.2}O$) with superior lithium storage performance. *J. Alloy. Compd.* **2019**, *777*, 767–774. [CrossRef]
27. Triolo, C.; Wenlei, X.; Petrovičovà, B.; Pinna, N.; Santangelo, S. Evaluation of Entropy-Stabilized $(Mg_{0.2}Co_{0.2}Ni_{0.2}Cu_{0.2}Zn_{0.2})O$ Oxides Produced via Solvothermal Method or Electrospinning as Anodes in Lithium-Ion Batteries. *Adv. Funct. Mater.* **2022**, *32*, 2202892. [CrossRef]
28. Tsai, M.-H.; Yeh, J.-W. High-Entropy Alloys: A Critical Review. *Mater. Res. Lett.* **2022**, *2*, 107–123. [CrossRef]
29. Guo, S.; Liu, C.T. Phase stability in high entropy alloys: Formation of solid-solution phase or amorphous phase. *Prog. Nat. Sci. Mater. Int.* **2011**, *21*, 433–446. [CrossRef]
30. Zhang, Y.; Zhou, Y.J.; Lin, J.P.; Chen, G.L.; Liaw, P.K. Solid-Solution Phase Formation Rules for Multi-component Alloys. *Adv. Energy Mater.* **2008**, *10*, 534–538. [CrossRef]
31. Toby, B.H.; Von Dreele, R.B. GSAS-II: The genesis of a modern open-source all purpose crystallography software package. *J. Appl. Crystallogr.* **2013**, *46*, 544–549. [CrossRef]
32. Toby, B.H. EXPGUI, a graphical user interface for GSAS. *J. Appl. Crystallogr.* **2004**, *34*, 210–213. [CrossRef]
33. Wang, Y.P.; Li, B.S.; Ren, M.X.; Fu, H.Z. Microstructure and compressive properties of AlCrFeCoNi high entropy alloy. *Mater. Sci. Eng. A* **2008**, *491*, 154–158. [CrossRef]
34. Wanderley, R.R.; Knuutila, H.K. Evaluating the possibility of high-pressure desorption of CO_2 via volatile co-solvent injection. *Chem. Eng. Res. Des.* **2021**, *169*, 116–134. [CrossRef]
35. Fracchia, M.; Manzoli, M.; Anselmi-Tamburini, U.; Ghigna, P. A new eight-cation inverse high entropy spinel with large configurational entropy in both tetrahedral and octahedral sites: Synthesis and cation distribution by X-ray absorption spectroscopy. *Scr. Mater.* **2020**, *188*, 26–31. [CrossRef]
36. Ma, S.; Ding, Q.; Wei, X.; Zhang, Z.; Bei, H. The Effects of Alloying Elements Cr, Al, and Si on Oxidation Behaviors of Ni-Based Superalloys. *Materials* **2022**, *15*, 7352. [CrossRef] [PubMed]
37. He, M.; Kang, H.; Lin, S.; Liu, Y.; Zhang, P.; Qin, W.; Wu, X. Impressive high-temperature oxidation resistance of FeCrNiMnAl high entropy alloy coating on the ferritic/martensitic steel with primordial Al_2O_3 and Mn_3O_4 gradient films. *J. Alloy. Compd.* **2022**, *928*, 167109. [CrossRef]
38. Ghadami, F.; Davoudabadi, M.A.; Ghadami, S. Cyclic Oxidation Properties of the Nanocrystalline AlCrFeCoNi High-Entropy Alloy Coatings Applied by the Atmospheric Plasma Spraying Technique. *Coatings* **2022**, *12*, 372. [CrossRef]
39. Zhang, F.; Wang, L.; Yan, S.; Yu, G.; Chen, J.; Yin, F. High temperature oxidation behavior of atmosphere plasma sprayed AlCoCrFeNi high-entropy alloy coatings. *Mat. Chem. Phys.* **2022**, *282*, 125939. [CrossRef]
40. Lu, J.; Li, L.; Chen, Y.; Liu, X.; Zhao, X.; Guo, F.; Xiao, P. Y-Hf co-doped AlCoCrFeNi high-entropy alloy coating with superior oxidation and spallation resistance at 1100 °C. *Corr. Sci.* **2021**, *182*, 109267. [CrossRef]
41. Prajapati, A.K.; Bhatnagar, A. A review on anode materials for lithium/sodim-ion batteries. *J. Energy Chem.* **2023**, *83*, 509–540. [CrossRef]

42. Sarkar, A.; Breitung, B.; Hahn, H. High entropy oxides: The role of entropy, enthalpy and synergy. *Scr. Mater.* **2020**, *187*, 43–48. [CrossRef]

43. Miracle, D.B.; Senkov, O.N. A critical review of high entropy alloys and related concepts. *Acta Mater.* **2017**, *122*, 448–511. [CrossRef]

44. Dippo, O.F.; Vecchio, K.S. A universal configurational entropy metric for high-entropy materials. *Scr. Mater.* **2021**, *201*, 113974. [CrossRef]

45. Wang, S.-Y.; Chen, T.-Y.; Kuo, C.-H.; Lin, C.-C.; Huang, S.-C.; Lin, M.-H.; Wang, C.-C.; Chen, H.-Y. Operando synchrotron transmission X-ray microscopy study on (Mg, Co, Ni, Cu, Zn)O high-entropy oxide anodes for lithium-ion batteries. *Mater. Chem. Phys.* **2021**, *274*, 125105. [CrossRef]

46. Xiao, B.; Wu, G.; Wang, T.; Wei, Z.; Sui, Y.; Shen, B.; Qi, J.; Wei, F.; Meng, Q.; Ren, Y.; et al. High entropy oxides $(FeNiCrMnX)_3O_4$ (X = Zn, Mg) as anode materials for lithium ion batteries. *Ceram. Int.* **2021**, *47*, 33972–33977. [CrossRef]

47. Wang, K.; Hua, W.; Huang, X.; Stenzel, D.; Wang, J.; Ding, Z.; Ciu, Y.; Wang, Q.; Ehrenberg, H.; Breitung, B.; et al. Synergy of cations in high entropy oxide lithium-ion battery anode. *Nat. Commun.* **2023**, *14*, 1487. [CrossRef]

48. Fracchia, M.; Callegari, D.; Coduri, M.; Anselmi-Tamburini, U.; Manzoli, M.; Quartarone, E.; Ghigna, P. Electrochemical performance of high and medium entropy oxides for lithium batteries. *Front. Energy Res.* **2022**, *10*, 883206. [CrossRef]

49. Liu, X.; Li, X.; Li, Y.; Zhang, H.; Jia, Q.; Zhang, S.; Lei, W. High-entropy oxide: A future anode contender for lithium-ion battery. *EcoMat* **2022**, *4*, e12261. [CrossRef]

50. Nguyen, T.X.; Tsai, C.-C.; Patra, J.; Clemens, O.; Chang, J.-K.; Ting, J.-M. Co-free high entropy spinel oxide anode with controlled morphology and crystallinity for outstanding charge/discharge performance in Lithium-ion batteries. *Chem. Eng. J.* **2022**, *430*, 132658. [CrossRef]

51. Illig, J. Physically Based Impedance Modelling of Lithium-Ion Cells. Ph.D. Thesis, Karlsruher Institut für Technologie, Karlsruhe, Germany, 4 April 2014. [CrossRef]

52. Illig, J.; Ender, M.; Chrobak, T.; Schmidt, J.P.; Klotz, D.; Ivers-Tiffée, E. Separation of Charge Transfer and Contact Resistance in $LiFePO_4$-Cathodes by Impedance Modeling. *J. Electrochem. Soc.* **2012**, *159*, A952. [CrossRef]

53. Shankar, L.S.; Zalka, D.; Szabó, T.; Székely, E.; Kőrösi, M.; Pászti, Z.; Balázsi, K.; Illés, L.; Czigány, Z.; Kun, R. Supercritical carbon dioxide assisted synthesis of ultra-stable sulfur/carbon composite cathodes for Li–S batteries. *Mater. Today Chem.* **2022**, *26*, 101240. [CrossRef]

54. Landesfeind, J.; Hattendorff, J.; Ehrl, A.; Wall, W.A.; Gasteiger, H.A. Tortuosity Determination of Battery Electrodes and Separators by Impedance Spectroscopy. *J. Electrochem. Soc.* **2016**, *163*, A1373. [CrossRef]

55. Wang, A.; Kadam, S.; Li, H.; Shi, S.; Qi, Y. Review on modeling of the anode solid electrolyte interphase (SEI) for lithium-ion batteries. *Npj Comput. Mater.* **2018**, *4*, 15. [CrossRef]

56. Chen, T.-Y.; Wang, S.-Y.; Kuo, C.-H.; Huang, S.-C.; Lin, M.-H.; Li, C.-H.; Chen, Y.-T.; Wang, C.-C.; Liao, Y.-F.; Lin, C.-C.; et al. In operando synchrotron X-ray studies of a novel spinel $(Ni_{0.2}Co_{0.2}Mn_{0.2}Fe_{0.2}Ti_{0.2})_3O_4$ high-entropy oxide for energy storage applications. *J. Mater. Chem. A* **2020**, *8*, 21756–21770. [CrossRef]

57. Kim, H.; Choi, W.; Yoon, J.; Um, J.H.; Lee, W.; Kim, J.; Cabana, J.; Yoon, W.-S. Exploring Anomalous Charge Storage in Anode Materials for Next-Generation Li Rechargeable Batteries. *Chem. Rev.* **2020**, *120*, 6934–6976. [CrossRef] [PubMed]

58. Vetter, J.; Novák, P.; Wagner, M.R.; Veit, C.; Möller, K.-C.; Besenhard, J.O.; Winter, M.; Wohlfahrt-Mehrens, M.; Vogler, C.; Hammouche, A. Ageing mechanisms in lithium-ion batteries. *J. Power Sources* **2005**, *147*, 269–281. [CrossRef]

59. Heubner, C.; Schneider, M.; Michaelis, A. Diffusion-Limited C-Rate: A Fundamental Principle Quantifying the Intrinsic Limits of Li-Ion Batteries. *Adv. Energy Mater.* **2019**, *10*, 1902523. [CrossRef]

60. Minouei, H.; Tsvetkov, N.; Kheradmandfard, M.; Han, J.; Kim, D.-E.; Hong, S.I. Tuning the electrochemical performance of high-entropy oxide nanopowder for anode Li-ion storage via structural tailoring. *J. Power Sources* **2022**, *549*, 232041. [CrossRef]

61. Lingappan, N.; Kong, L.; Pecht, M. The significance of aqueous binders in lithium-ion batteries. *Renew. Sust. Energ. Rev.* **2021**, *147*, 111227. [CrossRef]

62. Zhu, Z.; He, Y.; Hu, H.; Zhang, F. Evolution of Internal Stress in Heterogeneous Electrode Composite during the Drying Process. *Energies* **2021**, *14*, 1683. [CrossRef]

63. Yen, J.-Z.; Yang, Y.-C.; Tuan, H.Y. Interface engineering of high entropy Oxide@Polyaniline heterojunction enables highly stable and excellent lithium ion storage performance. *Chem. Eng. J.* **2022**, *450*, 137924. [CrossRef]